INTERNATIONAL JOURNAL FOR NUMERICAL AND ANALYTICAL METHODS IN GEOMECHANICS
Int. J. Numer. Anal. Meth. Geomech., **23,** 549–571 (1999)

THREE-DIMENSIONAL FINITE ELEMENT MODELLING FOR CONSOLIDATION DUE TO GROUNDWATER WITHDRAWAL IN A DESATURATING ANISOTROPIC AQUIFER SYSTEM

JUN-MO KIM[1,*,†] AND RICHARD R. PARIZEK[2,‡]

[1] *Department of Geological Sciences, Seoul National University, Seoul 151-742, Korea*
[2] *Department of Geosciences, Pennsylvania State University, University Park, PA 16802, U.S.A.*

SUMMARY

A poroelastic numerical model is presented to evaluate three-dimensional consolidation due to groundwater withdrawal from desaturating anisotropic porous media. This numerical model is developed based on the fully coupled governing equations for groundwater flow in deforming variably saturated porous media and the Galerkin finite element method. Two different cases of unsaturated aquifers are simulated for the purpose of comparison: a cross-anisotropic soil aquifer, and a corresponding isotropic soil aquifer composed of a geometrically averaged equivalent material. The numerical simulation results show that the anisotropy has a significant effect on the shapes of three-dimensional hydraulic head distribution and displacement vector fields. Such an effect of anisotropy is caused by the uneven partitioning of the hydraulic pumping stress between the vertical and horizontal directions in both groundwater flow field and solid skeleton deformation field. Copyright © 1999 John Wiley & Sons, Ltd.

Key words: cross-anisotropic soil; groundwater withdrawal; three-dimensional consolidation; poroelasticity theory; finite element model; numerical analysis

1. INTRODUCTION

Land deformation due to the withdrawal of groundwater and other fluid from porous media (e.g. soils and sedimentary rocks) is a well-known hydrogeomechanical phenomenon.[1,2] This phenomenon is sometimes referred to as consolidation. Groundwater extraction, which acts as a hydraulic stress, intrinsically induces the fully coupled hydraulic-mechanical interaction between water flow and solid skeleton (i.e. medium) deformation within an aquifer system as follows. As extraction of groundwater from an aquifer takes place, the pore water pressure decreases in the region of withdrawal. This leads to an increase in the effective stress acting on the

*Correspondence to: Jun-Mo Kim, Department of Geological Sciences, Seoul National University, Seoul 151-742, Korea
†Assistant Professor of Hydrogeology and Geomechanics
‡Professor of Hydrogeology

Contract grant sponsor: National Mine Land Reclamation Centre, West Virginia University; Mining and Mineral Resources Research Institute, Pennsylvania State University; Ministry of Education, Korea

CCC 0363–9061/99/060549–23$17.50

Received 30 April 1997
Revised 18 May 1998

solid skeleton, and consequently compaction of the aquifer medium (i.e. decrease in pore volume) occurs. This fully coupled hydraulic-mechanical phenomenon can be better explained through the poroelastic consolidation theory than the conventional theory of solid skeleton deformation that is uncoupled from groundwater flow.

Since the pioneering work of Biot,[3,4] the poroelasticity theory has been a widely accepted, valuable method for analysing various consolidation problems associated with fully coupled hydraulic-mechanical interaction between fluid flow and solid skeleton deformation in porous media. In his consolidation theory, a simultaneous solution is sought for the pore water pressure change and both vertical and horizontal displacements taking place in a three-dimensional system. Thus Biot's consolidation theory provides a more rigorous and realistic mathematical treatment for analysing the fully coupled groundwater flow and solid skeleton deformation due to groundwater withdrawal from porous media than Terzaghi's consolidation theory,[5] which is implemented as a two-step approach. As a result, Biot's consolidation theory has found fairly wide and practical applications in geomechanics, hydrogeology, and geotechnical engineering. Biot's poroelastic consolidation theory has also been further developed for entire flow regimes by others (e.g. References 6–8) using the modified effective stress concept[9] for unsaturated flow conditions.

On the basis of Biot's poroelastic consolidation theory, a variety of analytical solutions[10–12] and numerical solutions[13–19] have been presented to evaluate the fully coupled groundwater flow and solid skeleton deformation due to groundwater withdrawal from isotropic porous aquifer systems, which are fully or partially saturated. These analytical and numerical solutions are valid only for axially symmetric cylindrical systems which are bounded by concentric boundaries. This boundary condition is a reasonably good assumption for many cases, and certainly not a restriction. However, systems under consideration do not always have such concentric boundaries. A series of three-dimensional numerical simulations[20–22] was presented for multiphase fluid flow in deforming saturated hydrocarbon reservoirs. In addition, soils are generally deposited through a geologic process of sedimentation over a long period of time, and sometimes become sedimentary rocks. Under the resulting accumulative overburden pressure, soils display significant anisotropy with regard to hydraulic and mechanical properties. Hence, in order to describe the anisotropic nature of a soil, it must be modelled as a cross-anisotropic (transversely isotropic) porous medium whose hydraulic and mechanical properties are symmetric with respect to the vertical axis.[23–28] Thus a general three-dimensional poroelastic numerical model is desirable for more precise and practical analyses of the pore water pressure change and consolidation deformation due to groundwater withdrawal from porous aquifer systems with realistic settings such as non-concentric boundaries and anisotropic material properties.

The objectives of this paper are to quantitatively analyse the process of three-dimensional consolidation due to groundwater withdrawal from desaturating porous media and to evaluate the effect of anisotropy on such a hydrogeomechanical phenomenon, as an important application of the poroelasticity theory. In order to achieve these objectives, a set of fully coupled poroelastic governing equations and its numerical formulation are presented first. The numerical model is then verified by comparing simulation results with known analytical solutions for two fully saturated isotropic aquifer systems. Finally, unsaturated anisotropic and isotropic soil aquifer cases are simulated using the numerical model. Results from the numerical simulations of both cases are illustrated and compared to each other in order to provide a better understanding of the effect of anisotropy on three-dimensional consolidation due to groundwater withdrawal from a desaturating anisotropic aquifer system. From a practical point of view, a quantitative

understanding of the anisotropy effect may provide improved guidelines for predicting the long-term pore water pressure change and consolidation deformation induced by groundwater withdrawal under more realistic field conditions.

2. POROELASTIC GOVERNING EQUATIONS

A general mathematical model describing the pore water pressure change and land displacements due to groundwater withdrawal in a saturated-unsaturated porous medium may be formulated by combining the governing equations for groundwater flow and solid skeleton deformation.[6–8] These governing equations are derived based on the following basic assumptions: (1) the medium (solid skeleton) is porous and elastic while individual solid grains (soil particles) are incompressible, (2) the water is slightly compressible, (3) saturated-unsaturated water flow follows Darcy's law, (4) inertial force is neglected in force equilibrium equations, (5) the modified effective stress concept is valid for the entire saturated-unsaturated flow regime, and (6) the generalized Hooke's law holds for elastic deformation of the medium.

The governing equation for groundwater flow in a deforming variably saturated porous medium can be written as

$$\nabla \cdot [- \mathbf{K} \cdot \nabla(h + z)] + \left(n \frac{\mathrm{d}S_\mathrm{w}}{\mathrm{d}h} + nS_\mathrm{w}\beta_\mathrm{w}\gamma_\mathrm{w} \right) \frac{\partial h}{\partial t} + S_\mathrm{w} \frac{\partial}{\partial t} \left(\frac{\partial u_k}{\partial x_k} \right) = q \tag{1}$$

where $\mathbf{K} = K_{ij}$ is the second-order hydraulic conductivity tensor for $i, j = x, y, z$, $h = P/\gamma_\mathrm{w}$ is the pressure head, z is the vertical axis and elevation head, n is the porosity, S_w is the degree of water saturation, β_w is the compressibility of water, $\gamma_\mathrm{w} = \rho_\mathrm{w} g$ is the unit weight of water, u_k is the displacement of solid in the k direction, q is the water source or sink term, and t is time. Here P is the pore water pressure (positive for compression), ρ_w is the density of water, and g is the gravitational acceleration constant. Note that $\phi = h + z$ is the hydraulic head, $\mathrm{d}S_\mathrm{w}/\mathrm{d}h$ is the specific saturation capacity, $\theta_\mathrm{w} = nS_\mathrm{w}$ is the water content, and $\varepsilon_\mathrm{v} = \partial u_k/\partial x_k$ is the volume dilation or volumetric strain (positive for tension). In addition, $\mathbf{q}_r = - \mathbf{K} \cdot \nabla(h + z)$ is the Darcy velocity (flux).

The governing equation for solid skeleton deformation of a variably saturated porous medium can be expressed as

$$\frac{\partial}{\partial x_j} (\sigma'_{ij} - S_\mathrm{w}\gamma_\mathrm{w} h \delta_{ij})^e + f_i^e = 0, \quad i, j = x, y, z \tag{2a}$$

with

$$\sigma'^e_{ij} = C_{ijkl}\varepsilon_{kl}, \quad i, j, k, l = x, y, z \tag{2b}$$

where σ'_{ij} is the deformation-producing effective stress tensor (positive for tension), δ_{ij} is Kronecker's delta (1 if $i = j$, and 0 if $i \neq j$), $f_i = \rho_\mathrm{b} g_i = [nS_\mathrm{w}\rho_\mathrm{w} + (1 - n)\rho_\mathrm{s}] g_i$ is the component of body force acting in the i direction, ρ_b is the bulk density, ρ_s is the solid density, g_i is the component of gravitational acceleration in the i direction, C_{ijkl} is the fourth-order elasticity tensor, and $\varepsilon_{kl} = \partial u_k/\partial x_l + \partial u_l/\partial x_k (1 - \delta_{kl})$ is the strain tensor (positive for tension). The superscript e in equations (2a) and (2b) denotes the incremental values of physical quantities. For example, $h^e = h - h_0$ is the incremental pressure head in which h and h_0 are the current and initial pressure heads, respectively. Note that $\sigma_{ij} = \sigma'_{ij} - S_\mathrm{w}\gamma_\mathrm{w} h \delta_{ij}$ is the total stress tensor (positive for

tension) assuming that the Bishop's parameter or boundary porosity χ is approximately equal to the degree of water saturation S_w in the modified effective stress concept,[9] i.e. $\sigma_{ij} = \sigma'_{ij} - \chi\gamma_w h\delta_{ij} \approx \sigma'_{ij} - S_w\gamma_w h\delta_{ij}$. The number of independent elastic coefficients, which are necessary to formulate the elasticity tensor C_{ijkl}, is dependent upon the degree of mechanical anisotropy of the system. Nine, five, and two elastic coefficients should be known for mechanically anisotropic (orthotropic), cross-anisotropic (transversely isotropic), and isotropic systems, respectively.[29–31] The definitions of the elasticity tensor C_{ijkl} in equation (2b) for mechanically anisotropic, cross-anisotropic, and isotropic systems are listed in Appendix I. For example, equations (2a) and (2b) can be rewritten together for a mechanically isotropic system as

$$G\nabla^2 u_i + (\lambda + G)\frac{\partial}{\partial x_i}\left(\frac{\partial u_k}{\partial x_k}\right) + f_i^e = \frac{\partial}{\partial x_i}(S_w\gamma_w h)^e, \quad i = x, y, z \tag{3}$$

where $G = \mu = E/2(1 + v)$, $\lambda = Ev/(1 + v)(1 - 2v)$, G is the shear modulus (modulus of rigidity), E is Young's modulus (modulus of elasticity), and v is Poisson's ratio. The pair of constants λ and μ are often referred to as Lamé's constants.

Equations (1), (2a), and (2b) constitute a system of four non-linear partial differential governing equations with four dependent variables h, u_x, u_y, and u_z in Cartesian co-ordinates (x, y, z). Similarly, for axially symmetric cylindrical co-ordinates (r, z), three non-linear partial differential governing equations with three dependent variables h, u_r (radial displacement), and u_z can be derived by co-ordinate transformation (e.g. References 6, 10, and 11).

Meanwhile, in a deforming variably saturated porous medium, the water content θ_w and hydraulic conductivity tensor $\mathbf{K}$ in equations (1) and (2a) may be considered functions of both pore water pressure P and incremental effective stress tensor σ'^e_{ij} or, in turn, functions of pressure head h and resulting strain tensor ε_{ij} as follows:

$$\theta_w = \theta_w(P, \sigma'^e_{ij}) = \theta_w(h, \varepsilon_{ij}) = S_w(h)\, n(\varepsilon_{ij}) \tag{4}$$

$$\mathbf{K} = \mathbf{K}(P, \sigma'^e_{ij}) = \mathbf{K}(h, \varepsilon_{ij}) = K_r(h)\, \mathbf{K}_{sat}(\varepsilon_{ij}) \tag{5}$$

where K_r is the relative hydraulic conductivity, and $\mathbf{K}_{sat}$ is the saturated hydraulic conductivity tensor. In deriving equations (4) and (5), it is assumed that the unsaturated hydraulic properties (S_w and K_r) are unique functions of the pressure head h, whereas the saturated hydraulic properties (n and $\mathbf{K}_{sat}$) are unique functions of the strain tensor ε_{ij}.

3. NUMERICAL FORMULATION

As mentioned above, governing equations (1), (2a), and (2b) constitute a general mathematical statement of the physical problem of the pore water pressure change and land displacements due to groundwater withdrawal in variably saturated porous media. Unfortunately, a general analytical solution for this problem does not exit except for simplified cases. Numerical methods are the only tools that can be used to achieve general solutions for this problem. The Galerkin finite element method[32–34] is chosen here to approximate these governing equations because of its practical ability to handle anisotropic and heterogeneous regions with complex boundaries.

In the Galerkin finite element method, an unknown variable φ, which represents the pressure head h and the displacements u_x, u_y, and u_z in equations (1), (2a), and (2b), can be approximated

by a trial solution $\hat{\varphi}$ in space by means of the basis functions and their nodal values:

$$\varphi(x, y, z, t) \approx \hat{\varphi}(x, y, z, t) = \sum_{J=1}^{\mathrm{NN}} N_J(x, y, z)\,\varphi_J(t), \quad \varphi = h, u_x, u_y, u_z \tag{6}$$

where N_J is the basis function for node J, φ_J is the value of the unknown variable φ at node J, and NN is the total number of nodes in the region of interest. Application of the Galerkin finite element procedure and Green's theorem to equations (1) and (2a) yields the following equations:

$$\int_R \left\{\nabla N_I \cdot [\mathbf{K}\cdot\nabla(h+z)] + N_I\left(n\frac{\mathrm{d}S_\mathrm{w}}{\mathrm{d}h} + nS_\mathrm{w}\beta_\mathrm{w}\gamma_\mathrm{w}\right)\frac{\partial h}{\partial t} + N_I S_\mathrm{w}\frac{\partial}{\partial t}\left(\frac{\partial u_k}{\partial x_k}\right)\right\}\mathrm{d}R$$
$$= \int_R N_I q\,\mathrm{d}R + \int_B N_I \mathbf{n}\cdot[\mathbf{K}\cdot\nabla(h+z)]\,\mathrm{d}B, \quad I = 1, 2, 3, \ldots, \mathrm{NN} \tag{7}$$

$$\int_R \frac{\partial N_I}{\partial x_j}[\sigma'^e_{ij} - (S_\mathrm{w}\gamma_\mathrm{w}h\delta_{ij})^e]\,\mathrm{d}R = \int_R N_I f_i^e\,\mathrm{d}R + \int_B N_I \sigma_{ij}^e n_j\,\mathrm{d}B,$$
$$I = 1, 2, 3, \ldots, \mathrm{NN},\ i, j = x, y, z \tag{8}$$

where R is the domain of interest with boundary B, and n_j is the component of the outward unit vector $\mathbf{n}$ normal to the boundary B in the j direction. The incremental effective stress σ'^e_{ij} in equation (8) can then be expressed in terms of displacements by utilizing the elastic-constitutive relationship, i.e. equation (2b). Using equation (6) and recognizing that the basis functions are piecewise continuous over each element, equations (7) and (8) can be written together in a matrix form as

$$\begin{aligned}
&[C_{11}]\left\{\frac{\partial h}{\partial t}\right\} + [C_{12}]\left\{\frac{\partial u_x}{\partial t}\right\} + [C_{13}]\left\{\frac{\partial u_y}{\partial t}\right\} + [C_{14}]\left\{\frac{\partial u_z}{\partial t}\right\} + [C_{15}]\{h\} = \{R_1\}\\
&[C_{21}]\{h^e\} + [C_{22}]\{u_x\} + [C_{23}]\{u_y\} + [C_{24}]\{u_z\} = \{R_2\}\\
&[C_{31}]\{h^e\} + [C_{32}]\{u_x\} + [C_{33}]\{u_y\} + [C_{34}]\{u_z\} = \{R_3\}\\
&[C_{41}]\{h^e\} + [C_{42}]\{u_x\} + [C_{43}]\{u_y\} + [C_{44}]\{u_z\} = \{R_4\}
\end{aligned} \tag{9}$$

where $[C_{ij}]$ are the coefficient matrices, and $\{R_i\}$ are the load vectors. Here the subscripts i and j denote the number of governing equations and the number of dependent variables at each node, respectively. The definitions of the coefficient matrices and load vectors in equation (9) in Cartesian co-ordinates (x, y, z) and axially symmetric cylindrical co-ordinates (r, z) are given in Appendix II. The vector of incremental pressure head $\{h^e\}$ in equation (9) may be expressed as $\{h^e\} = \{h\}_t - \{h\}_{t=0}$ where $\{h\}_{t=0}$ is the value of pressure head prescribed at the initial time. Using this relationship and employing the finite difference scheme with a time weighting factor ω $(0 \leqslant \omega \leqslant 1)$ for the time derivative terms, equation (9) can be further written in a concise form as

$$[C^*]\{\varphi\} = \{R^*\} \tag{10}$$

where $[C^*] = [C^*_{ij}]$ is the global coefficient matrix, $\{R^*\} = \{R^*_i\}$ is the global load vector, and $\{\varphi\} = \{\{h\}^\mathrm{T}\{u_x\}^\mathrm{T}\{u_y\}^\mathrm{T}\{u_z\}^\mathrm{T}\}^\mathrm{T}$ is the unknown vector. The definitions of the global coefficient matrix and load vector in equation (10) are given in Appendix III.

Equations (1), (2a), and (2b) describe initial and boundary value problems. Thus the matrix equation (10) must be completely constrained by initial and boundary conditions before it is solved. Initial values of pressure head and displacements must be prescribed in the entire region of interest R. The boundary conditions associated with equation (10) are of the following four types: Dirichlet-type prescribed pressure head $h(t)$, Neumann-type prescribed normal flux to boundary $\mathbf{q}_r(t) = -\mathbf{n}\cdot[\mathbf{K}\cdot\nabla(h+z)]$, Dirichlet-type prescribed displacement in the i direction $u_i(t)$, and Neumann-type prescribed surface traction in the i direction $t_i(t) = \sigma^e_{ij}n_j$. In addition, mixed-type boundary conditions, which are combinations of the Dirichlet and Neumann boundary conditions, are sometimes necessary to treat more realistic situations occurring on the boundary. The variable rainfall-evaporation-seepage boundary condition is an example of such mixed-type boundary conditions. The numerical implementation of this mixed-type boundary condition was described in detail by Huyakorn *et al.*[35] and Yeh.[36]

In order to solve the non-linear problem associated with changes in the hydraulic properties due to unsaturated water flow and solid skeleton deformation at each time step, the incremental Picard scheme is adopted. It uses a non-linear iteration parameter Ω ($0 < \Omega \leqslant 2$) to stabilize non-linear iterations. For the next non-linear iteration level, the most recently updated nodal values of the dependent variables are used to compute the global coefficient matrix and load vector in equation (10). The non-linear iteration is continued until the numerical solution satisfies a specified convergence criterion (tolerance). At each non-linear iteration level, the linearized matrix equation can be solved by either the direct sparse matrix method[37] or one of the iterative NSPCG (non-symmetric preconditioned conjugate gradient) methods.[38]

4. MODEL VERIFICATION

Based on the finite element method described in the preceding section, a general multidimensional numerical model, named COWADE123D,[39] has been developed to solve the governing equations (1), (2a), and (2b) for a variety of fully coupled hydrogeomechanical phenomena in variably saturated porous media. This numerical model is verified for accuracy by comparing simulation results with known analytical solutions for two fully saturated isotropic aquifer systems as described below.[10,11]

4.1. Groundwater pumping from a saturated confined aquifer

In this model verification example, a fully penetrating well of radius r_w pumping at a constant rate Q_w from a saturated confined aquifer with infinite horizontal extent is considered (Figure 1). The aquifer is assumed to be homogeneous and isotropic in space and time. The aquifer system, fully saturated up to its top surface, is initially under hydrostatic equilibrium. The boundary at the pumping well bore ($r = r_w$) is restrained from any radial displacement, but it is free to move vertically. The aquifer system far from the pumping well ($r = \infty$) is not influenced by pumping. The impermeable bottom surface ($z = 0$) is fixed vertically, but it is free to move horizontally. The impermeable top surface ($z = B$) is free to move both vertically and horizontally. For such a case, Bear and Corapcioglu[10] derived the following analytical solution:

$$s = \frac{Q_w}{4\pi T} W(u) \tag{11}$$

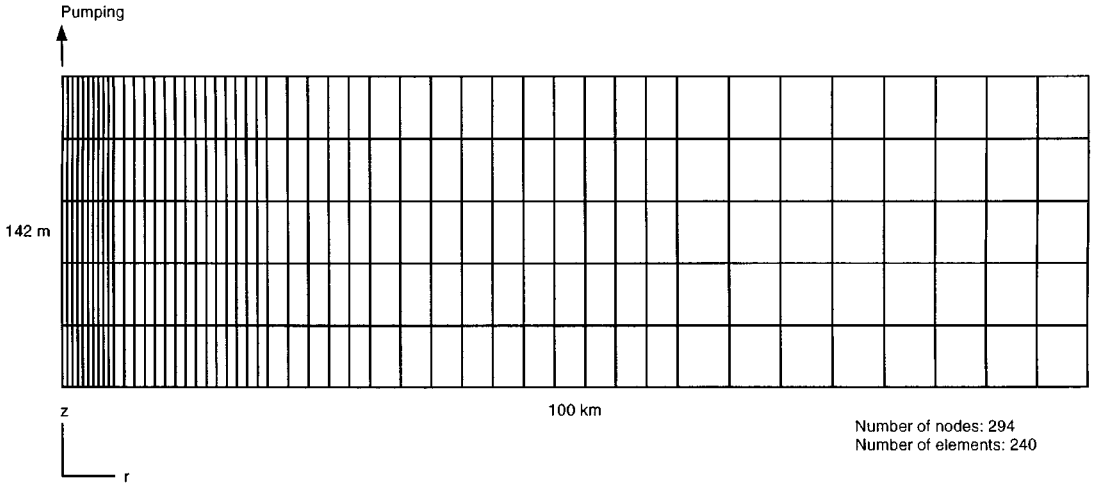

Figure 1. Finite element mesh used in the simulation of groundwater pumping from saturated confined and unconfined aquifers

$$\Delta z = -\frac{\gamma_w Q_w B}{8\pi T(\lambda + G)} W(u) \tag{12}$$

$$\bar{u}_r = -\frac{\gamma_w t Q_w C_v}{4\pi T r(\lambda + G)}[uW(u) + 1 - e^{-u}] \tag{13}$$

where $s = \phi_0 - \phi$ is the drawdown in which ϕ_0 is the initial hydraulic head, Δz is the vertical displacement at the top surface, $\bar{u}_r$ is the thickness-averaged radial displacement, $T = KB$ is the transmissivity, $S = B\gamma_w[n\beta_w + (\lambda + G)^{-1}]$ is the storativity, $C_v = T/S$ is the consolidation coefficient or hydraulic diffusivity of the confined aquifer, and $W(u) = \int_u^\infty e^{-x}/x\,dx$ is the well function in which $u = r^2/4C_v t = r^2 S/4Tt$. In deriving analytical solutions (11)–(13), the magnitude of the vertical displacement Δz at the top surface was assumed to be very small compared to the saturated thickness of the aquifer B, i.e. $B \gg \Delta z$, and hence $B \approx B_0$ in which B_0 is the initial saturated thickness of the aquifer.

The initial hydraulic head ϕ_0 is assigned everywhere to be equal to three times the aquifer thickness, i.e. $\phi_0 = 3B$. The saturated aquifer thickness B is set of equal to 142 m, and a fully penetrating well of radius $r_w = 0{\cdot}3$ m pumping at a constant rate $Q_w = 1{\cdot}0\ m^3/s$ is used in this verification example. A finite horizontal extent of 100 km is chosen to approximate the infinite horizontal domain (see Figure 1). The material properties of the confined aquifer are given as follows: $n = 0{\cdot}1$, $K = 6{\cdot}69 \times 10^{-5}$ m/s, $v = 0{\cdot}25$, and $E = 1{\cdot}12 \times 10^8\ N/m^2$. The compressibility of water β_w is neglected here, i.e. $\beta_w = 0$, and the unit weight of water γ_w is set equal to $9{\cdot}806 \times 10^3\ N/m^3$. The aquifer system is discretized into 240 ($= 48 \times 5$) isoparametric quadrilateral elements with 294 ($= 49 \times 6$) nodes (see Figure 1). A uniform time step size of 0·2 yr and 15 time steps are used in the numerical simulation. The time weighting factor ω is set equal to 1·0 (implicit backward time stepping). The direct sparse matrix method[37] is used to solve the matrix

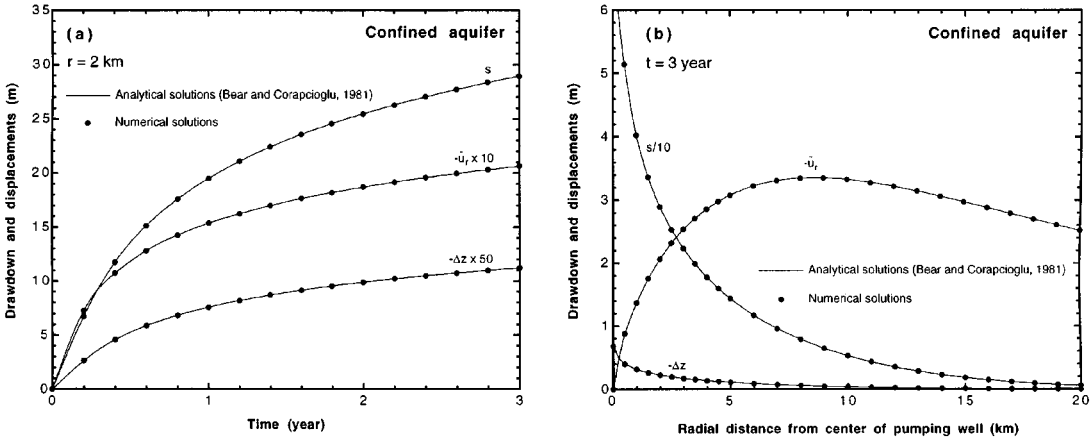

Figure 2. (a) Temporal changes and (b) spatial distributions of drawdown and displacements in the confined aquifer

equations. The numerical solutions are shown in Figure 2 and are compared with the analytical solutions (11)–(13). As shown in Figure 2, the numerical and analytical solutions show extremely good agreement. In Figure 2(b), the correlation coefficients r_c between the analytical and numerical solutions are 0·994, 0·994, and 0·995 for the drawdown s, the vertical displacement Δz, and the radial displacement $\bar{u}_r$, respectively.

4.2. Groundwater pumping from a saturated unconfined aquifer

In this model verification example, a fully penetrating well of radius r_w pumping at a constant rate Q_w from a saturated unconfined (phreatic or water table) aquifer with infinite horizontal extent is considered (Figure 1). The same assumptions and initial and boundary conditions that were used for the confined aquifer mentioned above are applied again to the unconfined aquifer except the hydraulic boundary condition for the top surface. In the unconfined aquifer, the pore water above the phreatic surface (water table) is released from the aquifer due to the decline of the water table. For such a case, Corapcioglu and Bear[11] derived the following analytical solutions:

$$s = \frac{Q_w}{4\pi T} W(u) \tag{14}$$

$$\Delta z = -\frac{\gamma_w Q_w B}{8\pi T}\left[\frac{1}{\lambda + G} + \frac{(\lambda + 2G)S_y}{2G(\lambda + G)}\right] W(u) \tag{15}$$

$$\bar{u}_r = -\frac{\gamma_w t Q_w C_v^{**}}{4\pi T r}\left[\frac{1}{\lambda + G} - \frac{\lambda S_y}{2G(\lambda + G)}\right][uW(u) + 1 - e^{-u}] \tag{16}$$

with

$$u = \frac{r^2}{4t[(S_y/T) + (1/C_v^*)]^{-1}} = \frac{r^2}{4tC_v^{**}} \tag{17}$$

$$C_v^* = K\left\{\gamma_w\left[n\beta_w + \frac{1}{\lambda + G} + \frac{S_y}{2(\lambda + G)}\right]\right\}^{-1} \tag{18}$$

where $S_y = \theta_{ws} - \theta_{wr}$ is the specific yield defined as the volume of water released per unit decline of water table per unit horizontal area, $\theta_{ws} = n$ is the saturated water content, θ_{wr} is the residual water content or field capacity, C_v^* is the hydraulic diffusivity, and C_v^{**} is the consolidation coefficient of the unconfied aquifer. In deriving the analytical solutions (14)–(16), the magnitudes of the drawdown of the water table s and the vertical displacement Δz at the top surface were assumed to be very small compared to the saturated thickness of the aquifer B, i.e. $B \gg s$, $B \gg \Delta z$, and hence $B \approx B_0$.

The initial hydraulic head is assigned everywhere to be equal to the aquifer thickness, i.e. $\phi_0 = B$. The same aquifer geometry, pumping well set-up, material properties, finite element mesh, time stepping scheme, and solution method used in the preceding verification example are used again in this verification example. The specific yield S_y is set equal to the porosity, i.e. $S_y = n$ which means that complete drainage takes place, and the residual water content θ_{wr} is zero above the water table. The numerical solutions are shown in Figure 3 and are compared with the analytical solutions (14)–(16). As shown in Figure 3, the numerical and analytical solutions show extremely good agreement. In Figure 3(b), the correlation coefficients r_c between the analytical and numerical solutions are 0·992, 0·993, and 0·991 for the drawdown s, the vertical displacement Δz, and the radial displacement $\bar{u}_r$, respectively. The magnitudes of the drawdown and displacements in the unconfined aquifer are relatively smaller than those in the preceding confined aquifer case under the same pumping rate. This is the result of water release in response to the drop of the phreatic surface (water table) due to pumping and the consequent decrease in the body force in the unconfined aquifer system.

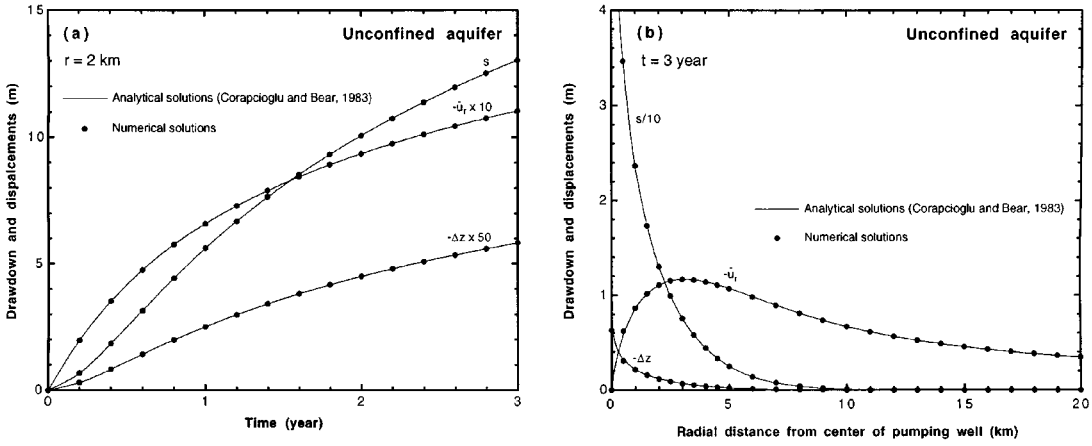

Figure 3. (a) Temporal changes and (b) spatial distributions of drawdown and displacements in the unconfined aquifer

5. MODEL APPLICATION

Two different (anisotropic and isotropic) cases of unsaturated aquifer systems are simulated using the numerical model that was successively verified in the preceding section to analyse the process of three-dimensional consolidation due to groundwater withdrawal from desaturating porous media and to evaluate the effect of anisotropy on such a hydrogeomechanical phenomenon.

5.1. Description of anisotropic aquifer and drainage well systems

This application example concerns groundwater flow into a system of vertical drainage wells fully penetrating a desaturating cross-anisotropic unconfined soil aquifer beneath a landfill site. The water table is initially located at a height of 22·5 m above the bottom surface of the aquifer. In order to lower the water table elevation below the base of the landfill, the drainage wells are placed at regular intervals of 400 m in the x direction and 300 m in the y direction between well centres as shown in Figure 4. The water level in the wells is then lowered suddenly to a height of 10 m, and this water level is maintained thereafter by groundwater pumping.

5.2. Initial and boundary conditions

Because of symmetry about the well centres, only a portion of the system (i.e. 200 m $\times$ 150 m $\times$ 25 m) is modelled (see Figure 4). Prior to start of the pumping, the aquifer system is at

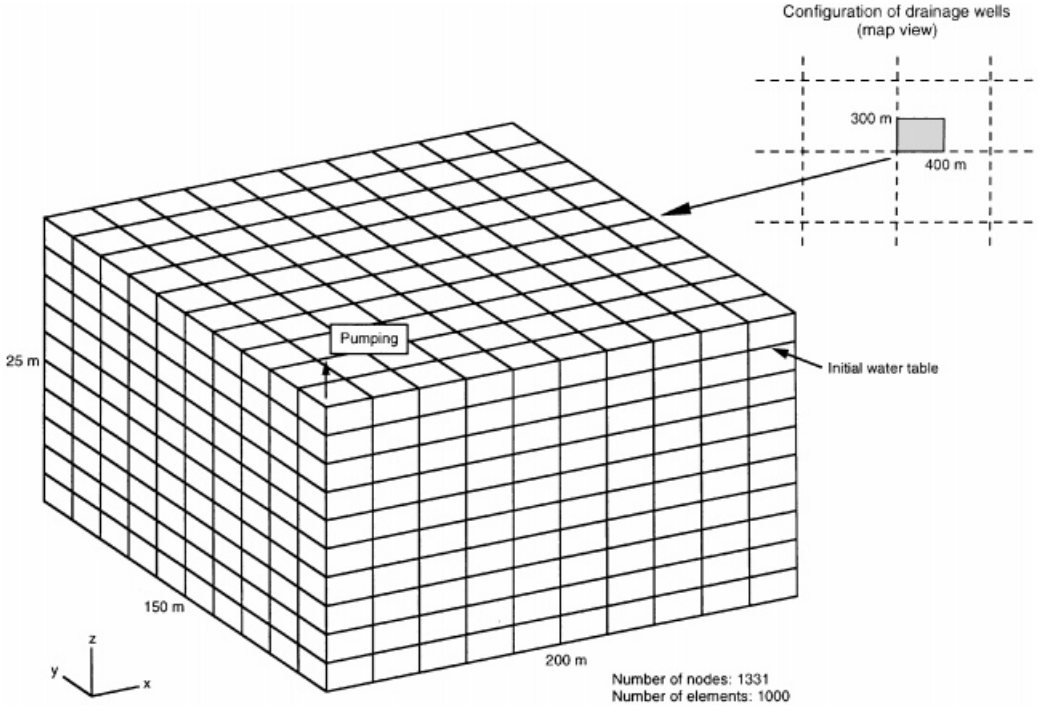

Figure 4. Finite element mesh used in the simulation of groundwater withdrawal from unsaturated anisotropic and isotropic aquifers

a hydrostatic equilibrium condition corresponding to the water table location, i.e. the initial hydraulic head ϕ_0 is everywhere equal to 22·5 m. Along the pumping well located at $x = 0$ m, a constant hydraulic head boundary condition of 10 m is applied for $0 \text{ m} \leqslant z \leqslant 10$ m. The top land surface located at $z = 25$ m is treated as permeable by applying a variable rainfall boundary condition with a rate of $6{\cdot}94 \times 10^{-8}$ m/s to take into account possible changes in infiltration rate caused by the pumping. For such a case, the maximum pressure head on the land surface is set equal to its initial value (i.e. $-2{\cdot}5$ m) in order to prevent a possible water table rise up to the land surface during the pumping because it is not likely to happen in most real situations. The land surface is also free to move both vertically and horizontally. A no-flow boundary condition is assigned on the four sides of the region. Boundary displacements in the x direction on the two sides located at $x = 0$ m and $x = 200$ m, and in the y direction on the other sides located at $y = 0$ m and $y = 150$ m are constrained. These no-flow and no-displacement boundary conditions on the four vertical sides are essential because they are imaginary boundaries produced by the surrounding vertical drainage wells. The impermeable bottom surface located at $z = 0$ m is fixed vertically, but it is free to move horizontally.

5.3. *Material properties of anisotropic aquifer and groundwater*

The material properties of the anisotropic aquifer described above are given in Table I, which were fabricated using some general information extracted from Tarn and Lu,[28] Huyakorn *et al.*,[35] and Huyakorn *et al.*.[40] These properties are typical of unconsolidated sandy and silty (loam)

Table I. Material properties of the anisotropic and isotropic aquifers used in the simulation

Parameter	Anisotropic aquifer	Isotropic aquifer
Initial porosity, n_0	0·25	0·25
Initial saturated hydraulic conductivity,		
$K_{\text{sat}_0 xx} = K_{\text{sat}_0 yy}$	$5{\cdot}79 \times 10^{-5}$ m/s	$3{\cdot}65 \times 10^{-5}$ m/s
$K_{\text{sat}_0 zz}$	$1{\cdot}45 \times 10^{-5}$ m/s	$3{\cdot}65 \times 10^{-5}$ m/s
Poisson's ratio,		
v_{xy}	0·099	0·25
$v_{xz} = v_{yz}$	0·396	0·25
Young's modulus,		
$E_x = E_y$	$2{\cdot}33 \times 10^7$ N/m^2	$1{\cdot}47 \times 10^7$ N/m^2
E_z	$5{\cdot}83 \times 10^6$ N/m^2	$1{\cdot}47 \times 10^7$ N/m^2
Shear modulus,		
G_{xy}	$1{\cdot}06 \times 10^7$ N/m^2*	$5{\cdot}88 \times 10^6$ N/m^2†
$G_{yz} = G_{zx}$	$2{\cdot}92 \times 10^6$ N/m^2	$5{\cdot}88 \times 10^6$ N/m^2†
Solid density, ρ_s	2.65×10^3 kg/m^3	2.65×10^3 kg/m^3
Residual water saturation, S_{wr}	0·05	0·05
Air-entry value, h_a	0·0 m	0·0 m
Unsaturated hydraulic parameters,		
α_{BV}	0·5 1/m	0·5 1/m
β_{BV}	2·0	2·0
γ_{BV}	1·0	1·0
n_{BV}	2·0	2·0

*$G_{xy} = E_x/2(1 + v_{xy})$
†$G = E/2(1 + v)$

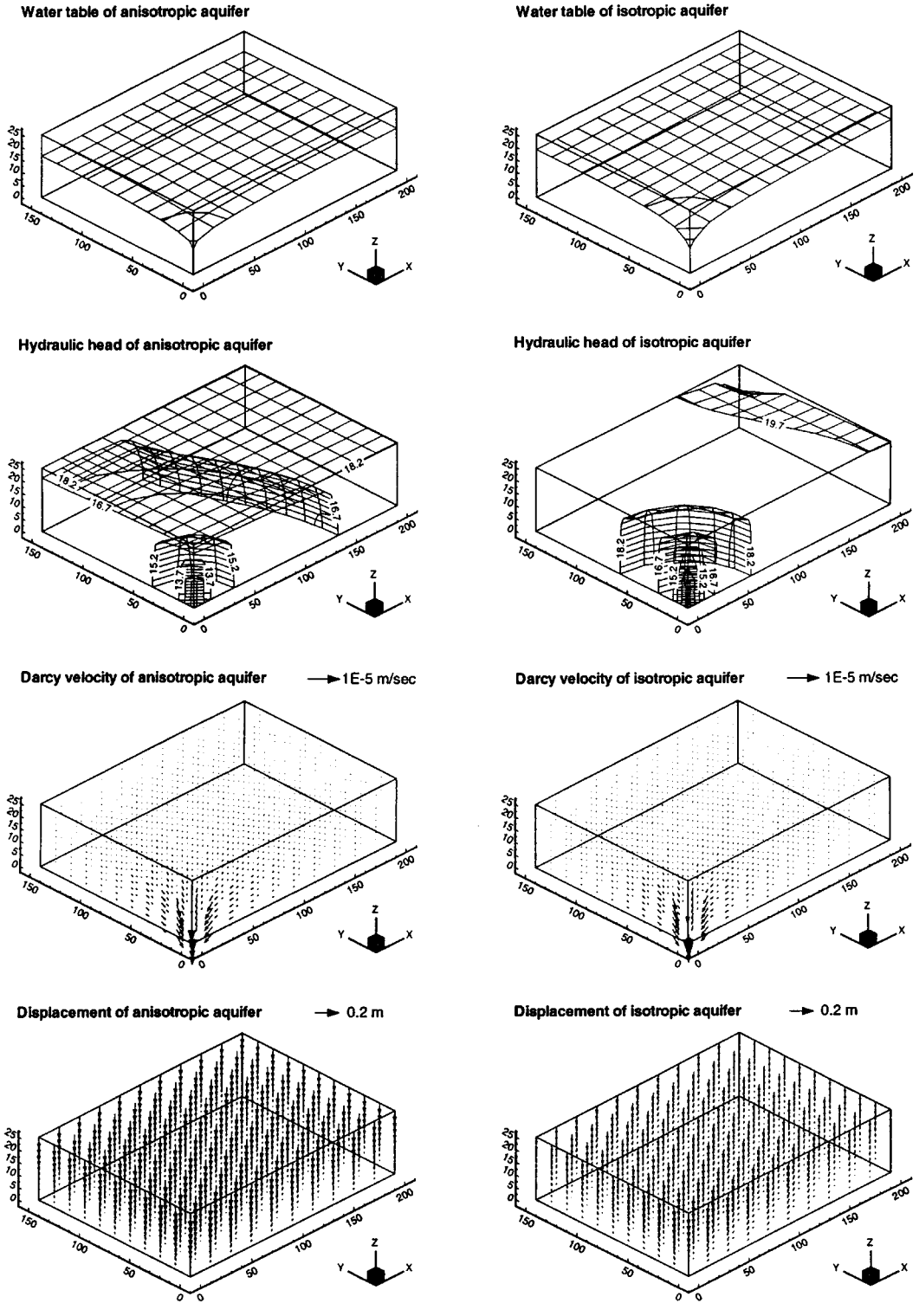

materials. The representative value of the solid density ρ_s is about $2{\cdot}65 \times 10^3$ kg/m^3, which is reasonably good approximation for most soils.[41] The following functional constitutive relationships are employed here to consider the unsaturated flow condition:[40]

$$S_w(h) = S_{wr} + (1 - S_{wr})[1 + (\alpha_{BV}|h - h_a|)^{\beta_{BV}}]^{-\gamma_{BV}}, \quad h < h_a \tag{19}$$

$$K_r(h) = [1 + (\alpha_{BV}|h - h_a|)^{\beta_{BV}}]^{-\gamma_{BV} n_{BV}}, \quad h < h_a \tag{20}$$

where S_{wr} is the residual water saturation, h_a is the air-entry value or bubbling pressure head, and α_{BV}, β_{BV}, cf. see γ_{BV}, and n_{BV} are the unsaturated hydraulic parameters. Equation (19) was taken from van Genuchten *et al.*,[42] whereas equation (20) was taken from Brooks and Corey[43] and Mualem.[44] Values of S_{wr}, h_a, α_{BV}, β_{BV}, γ_{BV}, and n_{BV} for the same soil are also given by Huyakorn *et al.*.[40] The specific saturation capacity term dS_w/dh in equation (1) can be obtained by differentiating equation (19) with respect to the pressure head h. A mathematical model is also employed here to account for the changes in the saturated hydraulic properties n and $\mathbf{K}_{sat}$ by the solid skeleton deformation:[45]

$$n(\varepsilon_{ij}) = 1 - \frac{1 - n_0}{1 + \varepsilon_v} \tag{21}$$

$$\mathbf{K}_{sat}(\varepsilon_{ij}) = \mathbf{K}_{sat_0}\left[\left(\frac{1}{n_0}\right)(1 + \varepsilon_v)^{2/3} - \left(\frac{1 - n_0}{n_0}\right)(1 + \varepsilon_v)^{-1/3}\right]^3 \tag{22}$$

where n_0 the initial porosity, and $\mathbf{K}_{sat_0}$ is the initial saturated hydraulic conductivity tensor prior to deformation. Equation (21) is based on the relationship between the porosity and the volumetric strain assuming that the individual solid grains are relatively incompressible compared to the solid skeleton. The same assumption has also been used by others (e.g. References 6–8) in deriving the groundwater flow governing equation (1). Equation (22) is obtained by substituting equation (21) into the Kozeny–Carman equation.[46–48] In equations (21) and (22), the volumetric strain ε_v is equal to $\partial u_x/\partial x + \partial u_y/\partial y + \partial u_z/\partial z$ for Cartesian co-ordinates (x, y, z) and $\partial u_r/\partial r + u_r/r + \partial u_z/\partial z$ for axially symmetric cylindrical co-ordinates (r, z). The compressibility of water β_w is set equal to $5{\cdot}0 \times 10^{-10}$ m^2/N, and the unit weight of water γ_w is set equal to $9{\cdot}806 \times 10^3$ N/m^3.

5.4. *Spatial and temporal discretizations and solution scheme*

The cross-anisotropic aquifer system is discretized into 1000 ($= 10 \times 10 \times 10$) isoparametric hexahedral elements with 1331 ($= 11 \times 11 \times 11$) nodes (see Figure 4). In the numerical simulation, the time step is initially set equal to 30 min, and it is then successively increased by a factor of 2 until it reaches 503 316 480 min. The total simulation time period is about 699 051 d (more exactly 1 006 632 930 min) after 25 time steps. Such a long time period is arbitrarily chosen to guarantee that the system arrives at the final steady-state condition in the numerical simulation because time required to do so is not known a priori. The time weighting factor ω is set equal to

Figure 5. Spatial distributions of water table, hydraulic head, Darcy velocity, and displacement vector in the anisotropic aquifer (left column) and isotropic aquifer (right column) at the final steady-state condition ($t > 7{\cdot}5$ yr). The units of hydraulic head and displacement vector are m, and the unit of Darcy velocity is m/s. The units of co-ordinate axes are m

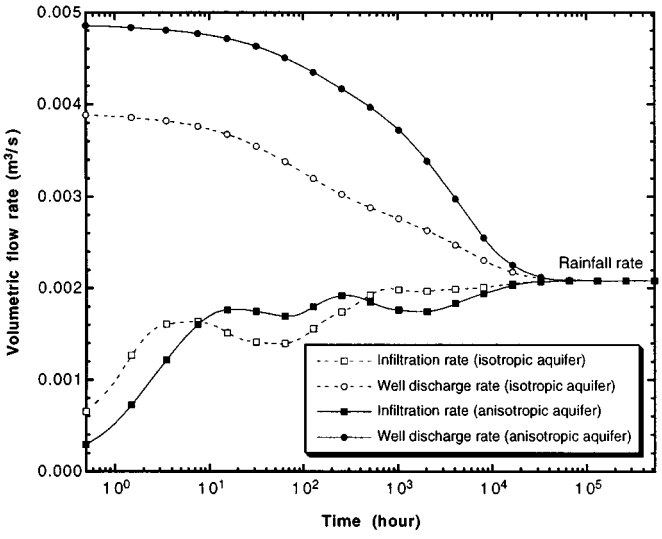

Figure 6. Temporal changes of well discharge and infiltration rates in the anisotropic and isotropic aquifers

1·0 (implicit backward time stepping), and the non-linear iteration parameter Ω is set equal to 0·5 (under-relaxation scheme) to prevent numerical oscillation. The convergence criteria (tolerances) for pressure head and displacements are set equal to 10^{-5} m for non-linear iterations and 10^{-6} m for linear iterations, while the linearized matrix equations are solved by the ICGMRES (incomplete Cholesky LU decomposed, generalized minimal residual) method among the NSPCG methods.[38]

5.5. *Results and analyses*

An unsaturated isotropic aquifer system is also simulated in this section for the purpose of comparison with the unsaturated cross-anisotropic aquifer system described above. The material properties of the isotropic aquifer system are obtained by taking geometric averages of those of the anisotropic aquifer system (see Table I). The same aquifer geometry, drainage well set-up, initial and boundary conditions, finite element mesh, time stepping scheme, and solution method that were used for the cross-anisotropic aquifer system are also applied to the isotropic aquifer system.

The spatial distributions of water table, hydraulic head, Darcy velocity, and displacement vector in the anisotropic aquifer system at the steady-state condition are shown in the left column in Figure 5 and are compared with those of the isotropic aquifer system (see the right column in Figure 5). It takes about 7·5 yr to arrive at the final steady-state condition after the start of pumping in both aquifer systems. Certain differences are observed in the hydrogeomechanical responses of the anisotropic and isotropic aquifer systems to groundwater pumping.

Figure 6 shows the temporal changes of well discharge and infiltration rates in both aquifer systems. The infiltration rate is initially smaller than the rainfall rate and eventually approaches to it. On the other hand, the well discharge rate is initially greater than the infiltration rate

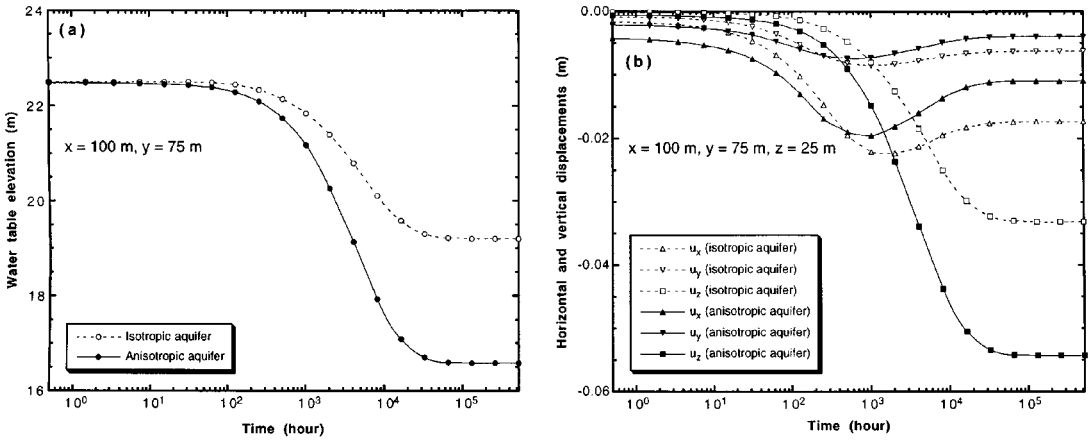

Figure 7. Temporal changes of (a) water table elevation from the bottom surface ($z = 0$ m) and (b) displacements on the land surface ($z = 25$ m) at $x = 100$ m and $y = 75$ m in the anisotropic and isotropic aquifers

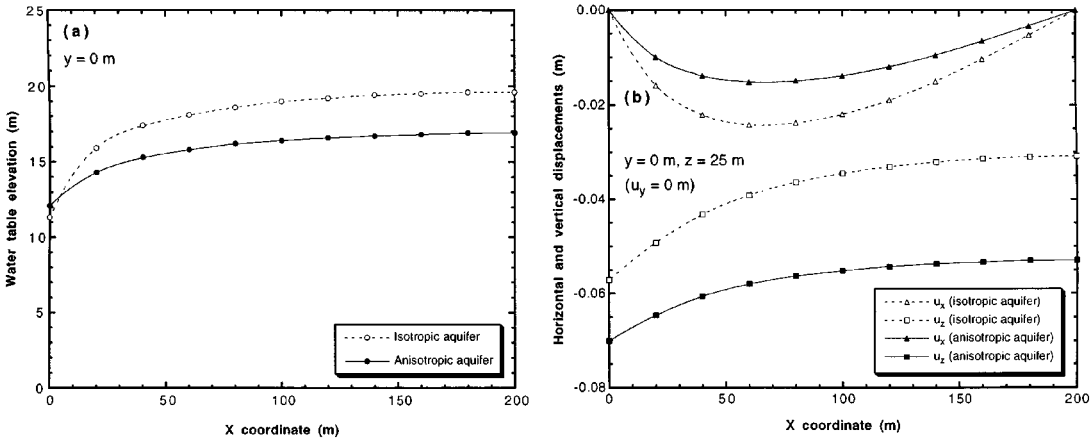

Figure 8. Profiles of (a) steady-state water table elevation from the bottom surface ($z = 0$ m) and (b) steady-state displacements on the land surface ($z = 25$ m) along the cross-section at $y = 0$ m in the anisotropic and isotropic aquifers

because infiltrating water is not the only source for the well discharge, and water stored in pores is also discharged to the well by pumping. As time progresses, the well discharge rate decreases, while the infiltration rate increases approaching each other. At the final steady-state condition, these two volumetric flow rates meet and become equal to the rainfall rate multiplied by the land surface area (i.e. $6{\cdot}94 \times 10^{-8}$ m/s $\times$ 200 m $\times$ 150 m $= 2{\cdot}082 \times 10^{-3}$ m^3/s). Note that the infiltration rate oscillates before it arrives at the rainfall rate in both cases of the aquifer systems. This aspect is an object of further investigation.

At $x = 100$ m and $y = 75$ m in both aquifer systems, the horizontal displacements u_x and u_y on the land surface ($z = 25$ m) first increase and then decrease, while the water table elevation, which is at $h = 0$ m, from the bottom surface ($z = 0$ m) and the vertical displacement u_z on the land

surface ($z = 25$ m) consistently decreases and increases, respectively, toward their respective final steady-state values as shown in Figure 7. The unexpected responses of the horizontal displacements are due to the presence of the surrounding drainage wells and the resulting imaginary side boundary conditions.

As shown in Figure 8(a), more water is extracted from the pores in the anisotropic aquifer system than the isotropic aquifer system, and hence the final steady-state water table of the anisotropic aquifer is more depleted and flattened than that of the isotropic aquifer. This results from the greater preferential groundwater flow in the horizontal direction than the vertical direction because the horizontal hydraulic conductivity $K_h = K_{xx} = K_{yy}$ is greater than the vertical hydraulic conductivity $K_v = K_{zz}$ in the anisotropic aquifer. Note that the length of the seepage face along the drainage well is determined to be approximately 2·1 m in the anisotropic aquifer system, whereas 1·3 m in the isotropic aquifer system. At the same time, more vertical displacement and less horizontal displacements are observed in the anisotropic aquifer compared to the displacement profile of the isotropic aquifer as shown in Figure 8(b). This is the result of the uneven partitioning of the pressure head decline, which is induced by the hydraulic pumping stress, between the vertical and horizontal directions because the vertical modulus $E_v = E_z$ is smaller than the horizontal modulus $E_h = E_x = E_y$ in the anisotropic aquifer.

6. CONCLUSIONS

A fully coupled poroelastic mathematical model and its finite element formulation have been presented to analyse the process of three-dimensional consolidation due to groundwater withdrawal from unsaturated porous media and to evaluate the effect of anisotropy on such a hydrogeomechanical phenomenon. The numerical model was successively verified against known analytical solutions for two simplified cases of saturated isotropic aquifers. The numerical model was then applied to unsaturated anisotropic and isotropic aquifer systems for the purpose of comparison. The material properties of the anisotropic and isotropic aquifer systems necessary for its model application were selected from the literature. The numerical simulation results shows that the anisotropy has its own importance not only in the groundwater flow field but also in the solid skeleton deformation field, and hence it cannot always be ignored especially when the long-term pore water pressure change and consolidation deformation induced by groundwater withdrawal are predicted. Therefore, it may be concluded that the anisotropy of the aquifer system must be properly considered if reasonable predictions of the long-term pore water pressure change and land deformation induced by groundwater withdrawal are to be obtained. Further numerical studies of various aquifer settings and field applications are recommended to arrive at more general conclusions concerning the effect of anisotropy on three-dimensional consolidation due to groundwater withdrawal from desaturating anisotropic soil aquifer systems.

ACKNOWLEDGEMENTS

This research was supported in part by the National Mine Land Reclamation Centre, West Virginia University and the Mining and Mineral Resources Research Institute, Pennsylvania State University. Partial support was also provided by the Ministry of Education, Korea, through the College of Natural Sciences, Seoul National University, under the 1997 Enhancement Project for Graduate Study. The authors are grateful to Dr. Derek Elsworth and Dr. Gour-Tsyh Yeh for

critical help in this manuscript preparation. The authors would also like to thank three anonymous reviewers for their valuable and constructive comments.

APPENDIX I

The elasticity tensor C_{ijkl} in equation (2b) for an anisotropic (orthotropic) system is defined using $v_{ij}/E_i = v_{ji}/E_j$ as[29–31]

$$C_{ijkl} = \begin{bmatrix} a & b & c & 0 & 0 & 0 \\ b & d & e & 0 & 0 & 0 \\ c & e & f & 0 & 0 & 0 \\ 0 & 0 & 0 & g & 0 & 0 \\ 0 & 0 & 0 & 0 & h & 0 \\ 0 & 0 & 0 & 0 & 0 & i \end{bmatrix}$$

with

$$a = \left(\frac{1}{E_y E_z} - \frac{v_{yz}^2}{E_y^2}\right)|\mathbf{D}|^{-1}$$

$$b = \left(\frac{v_{xy}}{E_x E_z} + \frac{v_{xz}v_{yz}}{E_x E_y}\right)|\mathbf{D}|^{-1}$$

$$c = \left(\frac{v_{xz}}{E_x E_y} + \frac{v_{xy}v_{yz}}{E_x E_y}\right)|\mathbf{D}|^{-1}$$

$$d = \left(\frac{1}{E_x E_z} - \frac{v_{xz}^2}{E_x^2}\right)|\mathbf{D}|^{-1}$$

$$e = \left(\frac{v_{xy}v_{xz}}{E_x^2} + \frac{v_{yz}}{E_x E_y}\right)|\mathbf{D}|^{-1}$$

$$f = \left(\frac{1}{E_x E_y} - \frac{v_{xy}^2}{E_x^2}\right)|\mathbf{D}|^{-1}$$

$$g = G_{xy}$$

$$h = G_{yz}$$

$$i = G_{zx}$$

$$|\mathbf{D}| = \frac{1}{E_x E_y E_z} - \frac{v_{xy}^2}{E_x^2 E_y} - \frac{v_{xz}^2}{E_x^2 E_y} - \frac{v_{yz}^2}{E_x E_y^2} - \frac{2v_{xy}v_{xz}v_{yz}}{E_x^2 E_y}$$

where E_i is Young's modulus (modulus of elasticity) in the i direction, v_{ij} is Poisson's ratio for normal strain in the j direction due to effective normal stress in the i direction, and G_{ij} is the shear modulus (modulus of rigidity) in the ij plane.

The elasticity tensor C_{ijkl} in equation (2b) for a cross-anisotropic (transversely isotropic) system with respect to the vertical z-axis is defined using $v_{xz} = v_{yz}$, $E_x = E_y$, and $G_{yz} = G_{zx}$ as[29–31]

$$C_{ijkl} = \begin{bmatrix} A+2N & A & F & 0 & 0 & 0 \\ A & A+2N & F & 0 & 0 & 0 \\ F & F & C & 0 & 0 & 0 \\ 0 & 0 & 0 & N & 0 & 0 \\ 0 & 0 & 0 & 0 & L & 0 \\ 0 & 0 & 0 & 0 & 0 & L \end{bmatrix}$$

with

$$A = \left(\frac{v_{xy}}{E_x E_z} + \frac{v_{xz}^2}{E_x^2}\right)|\mathbf{D}|^{-1}$$

$$F = \left(\frac{v_{xz}}{E_x^2} + \frac{v_{xy}v_{xz}}{E_x^2}\right)|\mathbf{D}|^{-1}$$

$$C = \left(\frac{1}{E_x^2} - \frac{v_{xy}^2}{E_x^2}\right)|\mathbf{D}|^{-1}$$

$$N = G_{xy} = \frac{E_x}{2(1+v_{xy})}$$

$$L = G_{yz} = G_{zx}$$

$$|\mathbf{D}| = \frac{1}{E_x^2 E_z} - \frac{v_{xy}^2}{E_x^2 E_z} - \frac{2v_{xz}^2}{E_x^3} - \frac{2v_{xy}v_{xz}^2}{E_x^3}$$

where $x = y = r$ in axially symmetric cylindrical co-ordinates (r, z).

The elasticity tensor C_{ijkl} in equation (2b) for an isotropic system is defined as[29–31]

$$C_{ijkl} = \begin{bmatrix} \lambda+2G & \lambda & \lambda & 0 & 0 & 0 \\ \lambda & \lambda+2G & \lambda & 0 & 0 & 0 \\ \lambda & \lambda & \lambda+2G & 0 & 0 & 0 \\ 0 & 0 & 0 & G & 0 & 0 \\ 0 & 0 & 0 & 0 & G & 0 \\ 0 & 0 & 0 & 0 & 0 & G \end{bmatrix}$$

with

$$\lambda = \frac{Ev}{(1+v)(1-2v)}$$

$$G = \mu = \frac{E}{2(1+v)}$$

where λ and μ are Lamé's constants.

APPENDIX II

Using the nine elastic coefficients (a, b, c, d, e, f, g, h, i) for an anisotropic (orthotropic) system (see Appendix I), the coefficient matrices and load vectors in equation (9) in Cartesian co-ordinates (x, y, z) are defined as

$$[C_{11}] = \int_R N_I \left(n \frac{\mathrm{d}S_\mathrm{w}}{\mathrm{d}h} + nS_\mathrm{w}\beta_\mathrm{w}\gamma_\mathrm{w} \right) N_J \,\mathrm{d}R$$

$$[C_{12}] = \int_R N_I S_\mathrm{w} \frac{\partial N_J}{\partial x} \,\mathrm{d}R$$

$$[C_{13}] = \int_R N_I S_\mathrm{w} \frac{\partial N_J}{\partial y} \,\mathrm{d}R$$

$$[C_{14}] = \int_R N_I S_\mathrm{w} \frac{\partial N_J}{\partial z} \,\mathrm{d}R$$

$$[C_{15}] = \int_R \nabla N_I \cdot \mathbf{K} \cdot \nabla N_J \,\mathrm{d}R$$

$$[C_{21}] = \int_R -\frac{\partial N_I}{\partial x} S_\mathrm{w}\gamma_\mathrm{w} N_J \,\mathrm{d}R$$

$$[C_{22}] = \int_R \left[\frac{\partial N_I}{\partial x} a \frac{\partial N_J}{\partial x} + \frac{\partial N_I}{\partial y} g \frac{\partial N_J}{\partial y} + \frac{\partial N_I}{\partial z} i \frac{\partial N_J}{\partial z} \right] \mathrm{d}R$$

$$[C_{23}] = \int_R \left[\frac{\partial N_I}{\partial x} b \frac{\partial N_J}{\partial y} + \frac{\partial N_I}{\partial y} g \frac{\partial N_J}{\partial x} \right] \mathrm{d}R$$

$$[C_{24}] = \int_R \left[\frac{\partial N_I}{\partial x} c \frac{\partial N_J}{\partial z} + \frac{\partial N_I}{\partial z} i \frac{\partial N_J}{\partial x} \right] \mathrm{d}R$$

$$[C_{31}] = \int_R -\frac{\partial N_I}{\partial y} S_\mathrm{w}\gamma_\mathrm{w} N_J \,\mathrm{d}R$$

$$[C_{32}] = \int_R \left[\frac{\partial N_I}{\partial x} g \frac{\partial N_J}{\partial y} + \frac{\partial N_I}{\partial y} b \frac{\partial N_J}{\partial x} \right] \mathrm{d}R$$

$$[C_{33}] = \int_R \left[\frac{\partial N_I}{\partial x} g \frac{\partial N_J}{\partial x} + \frac{\partial N_I}{\partial y} d \frac{\partial N_J}{\partial y} + \frac{\partial N_I}{\partial z} h \frac{\partial N_J}{\partial z} \right] \mathrm{d}R$$

$$[C_{34}] = \int_R \left[\frac{\partial N_I}{\partial y} e \frac{\partial N_J}{\partial z} + \frac{\partial N_I}{\partial z} h \frac{\partial N_J}{\partial y} \right] \mathrm{d}R$$

$$[C_{41}] = \int_R -\frac{\partial N_I}{\partial z} S_\mathrm{w}\gamma_\mathrm{w} N_J \,\mathrm{d}R$$

$$[C_{42}] = \int_R \left[\frac{\partial N_I}{\partial x} i \frac{\partial N_J}{\partial z} + \frac{\partial N_I}{\partial z} c \frac{\partial N_J}{\partial x} \right] \mathrm{d}R$$

$$[C_{43}] = \int_R \left[\frac{\partial N_I}{\partial y} h \frac{\partial N_J}{\partial z} + \frac{\partial N_I}{\partial z} e \frac{\partial N_J}{\partial y} \right] \mathrm{d}R$$

$$[C_{44}] = \int_R \left[\frac{\partial N_I}{\partial x} i \frac{\partial N_J}{\partial x} + \frac{\partial N_I}{\partial y} h \frac{\partial N_J}{\partial y} + \frac{\partial N_I}{\partial z} f \frac{\partial N_J}{\partial z} \right] \mathrm{d}R$$

$$\{R_1\} = \int_R - \nabla N_I \cdot \mathbf{K} \cdot \nabla z \, \mathrm{d}R + \int_R N_I q \, \mathrm{d}R + \int_B N_I \mathbf{n} \cdot [\mathbf{K} \cdot \nabla (h + z)] \, \mathrm{d}B$$

$$\{R_2\} = \int_R N_I f_x^e \, \mathrm{d}R + \int_B N_I (\sigma_{xx}^e n_x + \sigma_{xy}^e n_y + \sigma_{xz}^e n_z) \, \mathrm{d}B$$

$$\{R_3\} = \int_R N_I f_y^e \, \mathrm{d}R + \int_B N_I (\sigma_{yx}^e n_x + \sigma_{yy}^e n_y + \sigma_{yz}^e n_z) \, \mathrm{d}B$$

$$\{R_4\} = \int_R N_I f_z^e \, \mathrm{d}R + \int_B N_I (\sigma_{zx}^e n_x + \sigma_{zy}^e n_y + \sigma_{zz}^e n_z) \, \mathrm{d}B$$

where $\mathrm{d}R = \mathrm{d}x \, \mathrm{d}y \, \mathrm{d}z$.

Using the five elastic coefficients (A, C, F, L, N) for a cross-anisotropic (transversely isotropic) system (see Appendix I), the coefficient matrices and load vectors in equation (9) in axially symmetric cylindrical co-ordinates (r, z) are also defined as

$$[C_{11}] = \int_R N_I \left(n \frac{\mathrm{d}S_w}{\mathrm{d}h} + n S_\mathrm{w} \beta_\mathrm{w} \gamma_\mathrm{w} \right) N_J \, \mathrm{d}R$$

$$[C_{12}] = \int_R N_I S_\mathrm{w} \left[\frac{\partial N_J}{\partial r} + \frac{N_J}{r} \right] \mathrm{d}R$$

$$[C_{13}] = \mathbf{0}$$

$$[C_{14}] = \int_R N_I S_\mathrm{w} \frac{\partial N_J}{\partial z} \mathrm{d}R$$

$$[C_{15}] = \int_R \nabla N_I \cdot \mathbf{K} \cdot \nabla N_J \, \mathrm{d}R$$

$$[C_{21}] = \int_R - \left[\frac{\partial N_I}{\partial r} + \frac{N_I}{r} \right] S_\mathrm{w} \gamma_\mathrm{w} N_J \, \mathrm{d}R$$

$$[C_{22}] = \int_R \left[\frac{\partial N_I}{\partial r} (A + 2N) \frac{\partial N_J}{\partial r} + \frac{\partial N_I}{\partial r} A \frac{N_J}{r} + \frac{N_I}{r} (A + 2N) \frac{N_J}{r} + \frac{N_I}{r} A \frac{\partial N_J}{\partial r} + \frac{\partial N_I}{\partial z} L \frac{\partial N_J}{\partial r} \right] \mathrm{d}R$$

$$[C_{23}] = \mathbf{0}$$

$$[C_{24}] = \int_R \left[\frac{\partial N_I}{\partial r} F \frac{\partial N_J}{\partial z} + \frac{N_I}{r} F \frac{\partial N_J}{\partial z} + \frac{\partial N_I}{\partial z} L \frac{\partial N_J}{\partial r} \right] \mathrm{d}R$$

$$[C_{31}] = \mathbf{0}$$

$$[C_{32}] = \mathbf{0}$$

$$[C_{33}] = \mathbf{I}$$

$$[C_{34}] = \mathbf{0}$$

$$[C_{41}] = \int_R -\frac{\partial N_I}{\partial z} S_w \gamma_w N_J \, dR$$

$$[C_{42}] = \int_R \left[\frac{\partial N_I}{\partial r} L \frac{\partial N_J}{\partial z} + \frac{\partial N_I}{\partial z} F \frac{\partial N_J}{\partial r} + \frac{\partial N_I}{\partial z} F \frac{N_J}{r} \right] dR$$

$$[C_{43}] = \mathbf{0}$$

$$[C_{44}] = \int_R \left[\frac{\partial N_I}{\partial r} L \frac{\partial N_J}{\partial r} + \frac{\partial N_I}{\partial z} C \frac{\partial N_J}{\partial z} \right] dR$$

$$\{R_1\} = \int_R -\nabla N_I \cdot \mathbf{K} \cdot \nabla z \, dR + \int_R N_I q \, dR + \int_B N_I \mathbf{n} \cdot [\mathbf{K} \cdot \nabla (h + z)] \, dB$$

$$\{R_2\} = \int_R N_I f_r^e \, dR + \int_B N_I [\sigma_{rr}^e n_r + \sigma_{rz}^e n_z] \, dB$$

$$\{R_3\} = \mathbf{0}$$

$$\{R_4\} = \int_R N_I f_z^e \, dR + \int_B N_I [\sigma_{Zr}^e n_r + \sigma_{zz}^e n_z] \, dB$$

where $dR = r \, dr \, dz$, $\mathbf{I}$ is the identity matrix, and $\mathbf{0}$ stands for the matrix or vector in which all entries are zero. Here x and r co-ordinates are set to be equal assuming that $\{u_y\} = \mathbf{0}$.

APPENDIX III

The coefficient matrices and load vectors in equation (10) are defined as

$$[C_{11}^*] = \frac{[C_{11}]}{\Delta t} + \omega [C_{15}]$$

$$[C_{1j}^*] = \frac{[C_{1j}]}{\Delta t}, \quad j = 2, 3, 4$$

$$[C_{ij}^*] = [C_{ij}], \quad i = 2, 3, 4, \quad j = 1, 2, 3, 4$$

$$\{R_1^*\} = \{R_1\} + \left[\frac{[C_{11}]}{\Delta t} - (1 - \omega)[C_{15}] \right] \{h\}_{t - \Delta t} + \frac{[C_{12}]}{\Delta t} \{u_x\}_{t - \Delta t} + \frac{[C_{13}]}{\Delta t} \{u_y\}_{t - \Delta t} + \frac{[C_{14}]}{\Delta t} \{u_z\}_{t - \Delta t}$$

$$\{R_i^*\} = \{R_i\} + [C_{i1}]_{t=0} \{h\}_{t=0}, \quad i = 2, 3, 4$$

where Δt is the time step size, and ω is the time weighting factor ($0 \leqslant \omega \leqslant 1$).

REFERENCES

1. J. F. Poland, *Guidebook to Studies of Land Subsidence Due to Ground-Water Withdrawal*, *Studies and Reports in Hydrology*, Vol. 40, The United Nations Educational Scientific and Cultural Organization, Paris, 1984, 305 pp.
2. G. V. Chilingarian, E. C. Donaldson and T. F. Yen, *Subsidence Due to Fluid Withdrawal*, *Developments in Petroleum Science*, Vol. 41, Elsevier Science, Amsterdam, 1995, 498 pp.
3. M. A. Biot, 'General theory of three-dimensional consolidation', *J. Appl. Phys.*, **12,** 155–164 (1941).
4. M. A. Biot, 'Theory of elasticity and consolidation of a porous anisotropic soil', *J. Appl. Phys.*, **26,** 182–185 (1955).
5. K. Terzaghi, *Erdbaumechanik auf bodenphysikalischer Grundlage*, Franz Deuticke, Leipzig und Wien, 1925, 399 pp.
6. A. Verruijt, 'Elastic storage of aquifers', in R. J. M. De Wiest (ed.), *Flow Through Porous Media*, Academic Press, New York, 1969, pp. 331–376.
7. J. Bear and M. Y. Corapcioglu, 'Centrifugal filtration in deformable porous media', in *Water Flow in Deformable Porous Media*, *Report*, Department of Civil Engineering, University of Michigan, Ann Arbor, Michigan, 1981.
8. J. Noorishad, M. Mehran and T. N. Narasimhan, 'On the formulation of saturated-unsaturated fluid flow in deformable porous media', *Adv. Water Resour.*, **5,** 61–62 (1982).
9. A. W. Bishop and G. E. Blight, 'Some aspects of effective stress in saturated and partly saturated soils', *Geotechnique*, **13,** 177–197 (1963).
10. J. Bear and M. Y. Corapcioglu, 'Mathematical model for regional land subsidence due to pumping, 2. Integrated aquifer subsidence equations for vertical and horizontal displacements', *Water Resour. Res.*, **17,** 947–958 (1981).
11. M. Y. Corapcioglu and J. Bear, 'A mathematical model for regional land subsidence due to pumping, 3. Integrated equations for a phreatic aquifer', *Water Resour. Res.*, **19,** 895–908 (1983).
12. J. R. Booker and J. P. Carter, 'Analysis of a point sink embedded in a porous elastic half space', *Int. J. Numer. Anal. Meth. Geomech.*, **10,** 137–150 (1986).
13. N. M. Safai and G. F. Pinder, 'Vertical and horizontal land deformation in a desaturating porous medium', *Adv. Water Resour.*, **2,** 19–25 (1979).
14. N. M. Safai and G. F. Pinder, 'Vertical and horizontal land deformation due to fluid withdrawal', *Int. J. Numer. Anal. Meth. Geomech.*, **4,** 131–142 (1980).
15. R. W. Lewis and B. A. Schrefler, *The Finite Element Method in the Deformation and Consolidation of Porous Media*, Wiley, New York, 1987, 344 pp.
16. R. W. Lewis, B. A. Schrefler and L. Simoni, 'Coupling versus uncoupling in soil consolidation', *Int. J. Numer. Anal. Meth. Geomech.*, **15,** 533–548 (1991).
17. R. H. Lu, H. D. Yeh and G. T. Yeh, 'Finite element modeling for land displacements due to pumping', in C. Y. Kuo (ed.), *Engineering Hydrology*, American Society of Civil Engineers, New York, 1993, pp. 904–909.
18. J. P. Hsi, J. P. Carter and J. C. Small, 'Surface subsidence and drawdown of the water table due to pumping', *Geotechnique*, **44,** 381–396 (1994).
19. H. D. Yeh, R. H. Lu and G. T. Yeh, 'Finite element modelling for land displacements due to pumping', *Int. J. Numer. Anal. Meth. Geomech.*, **20,** 79–99 (1996).
20. R. W. Lewis and Y. Sukirman, 'Finite element modelling of three-phase flow in deforming saturated oil reservoirs', *Int. J. Numer. Anal. Meth. Geomech.*, **17,** 577–598 (1993).
21. Y. Sukirman and R. W. Lewis, 'A finite element solution of a fully coupled implicit formulation for reservoir simulation', *Int. J. Numer. Anal. Meth. Geomech.*, **17,** 677–698 (1993).
22. R. W. Lewis and Y. Sukirman, 'Finite element modelling for simulating the surface subsidence above a compacting hydrocarbon reservoir', *Int. J. Numer. Anal. Meth. Geomech.*, **18,** 619–639 (1994).
23. L. Barden, 'Stresses and displacements in a cross-anisotropic soil', *Geotechnique*, **13,** 198–210 (1963).
24. R. E. Gibson, 'The analytical method in soil mechanics', *Geotechnique*, **24,** 115–140 (1974).
25. J. Sekowski, 'Stratified subsoil modelled by a cross-anisotropic elastic half-space', *Int. J. Numer. Anal. Meth. Geomech.*, **10,** 407–414 (1986).
26. J. R. Booker and J. P. Carter, 'Elastic consolidation around a point sink embedded in a half-space with anisotropic permeability', *Int. J. Numer. Anal. Meth. Geomech.*, **11,** 61–77 (1987).
27. K. M. Lee and R. K. Rowe, 'Deformations caused by surface loading and tunnelling: The role of elastic anisotropy', *Geotechnique*, **39,** 125–140 (1989).
28. J. Q. Tarn and C. C. Lu, 'Analysis of subsidence due to a point sink in an anisotropic porous elastic half space', *Int. J. Numer. Anal. Meth. Geomech.*, **15,** 573–592 (1991).
29. A. E. H. Love, *A Treatise on the Mathematical Theory of Elasticity*, 4th edn., Dover, New York, 1944, 643 pp.
30. I. S. Sokolnikoff, *Mathematical Theory of Elasticity*, 2nd edn., McGraw-Hill, New York, 1956, 476 pp.

31. R. E. Goodman, *Introduction to Rock Mechanics*, Wiley, New York, 1980, 478 pp.
32. K. H. Huebner, *The Finite Element Methods for Engineers*, Wiley, New York, 1975, 500 pp.
33. P. S. Huyakorn and G. F. Pinder, *Computational Methods in Subsurface Flow*, Academic Press, New York, 1983, 473 pp.
34. J. Istok, *Groundwater Modeling by the Finite Element Method*, *Water Resources Monograph Series*, Vol. 13, American Geophysical Union, Washington, D.C., 1989, 495 pp.
35. P. S. Huyakorn, E. P. Springer, V. Guvanasen and T. D. Wadsworth, 'A three-dimensional finite-element model for simulating water flow in variably saturated porous media', *Water Resour. Res.*, **22,** 1790–1808 (1986).
36. G. T. Yeh, 'FEMWATER: A finite element model of water flow through saturated-unsaturated porous media — first revision', *Report ORNL-55671/R1*, Oak Ridge National Laboratory, Oak Ridge, Tennessee, 1987, 258 pp.
37. I. S. Duff, 'MA28—A set of FORTRAN subroutines for sparse unsymmetric linear equations', *AERE Harwell Report R-8730*, Atomic Energy Research Establishment, Harwell, England, 1977, 153 pp.
38. T. C. Oppe, W. D. Joubert and D. R. Kincaid, 'NSPCG user's guide version 1·0: A package for solving large sparse linear systems by various iterative methods', *Report CNA-216*, Center for Numerical Analysis, University of Texas, Austin, Texas, 1988, 82 pp.
39. J. M. Kim, 'COWADE123D: A finite element model for fully coupled saturated-unsaturated water flow in deforming one-, two-, and three-dimensional porous and fractured media', *Technical Report HGL-1995-9*, Hydrogeology Laboratory, Department of Geosciences, Pennsylvania State University Park, Pennsylvania, 1995, 254 pp.
40. P. S. Huyakorn, S. D. Thomas and B. M. Thompson, 'Techniques for making finite elements competitive in modeling flow in variably saturated porous media', *Water Resour. Res.*, **20,** 1099–1115 (1984).
41. R. A. Freeze and J. A. Cherry, *Groundwater*, Prentice-Hall, Englewood Cliffs, New Jersey, 1979, 604 pp.
42. M. Th. van Genuchten, G. F. Pinder and W. P. Saukin, 'Modeling of leachate and interactions in an aquifer', in S. K. Banerji (ed.), *Management of Gas and Leachate in Landfills*, *Report EPA-600/9-77-026*, U.S. Environmental Protection Agency, Cincinnati, Ohio, 1977, pp. 95–103.
43. R. H. Brooks and A. T. Corey, 'Hydraulic properties of porous media', *Hydrology Papers No. 3*, Colorado State University, Fort Collins, Colorado, 1964, 27 pp.
44. Y. Mualem, 'A new model for predicting the hydraulic conductivity of unsaturated porous media', *Water Resour. Res.*, **12,** 513–522 (1976).
45. J. M. Kim, 'A fully coupled model for saturated-unsaturated fluid flow in deformable porous and fractured media', *Ph.D. Thesis*, Pennsylvania State University, University Park, Pennsylvania, 1996, 201 pp.
46. J. Kozeny, 'Über kapillare Leitung des Wassers im Boden', *Sitzungsber. Akad. Wiss. Wien*, **136,** 271–306 (1927).
47. P. C. Carman, 'Fluid flow through granular beds', *Trans. Inst. Chem. Engrs.*, **15,** 150–166 (1937).
48. P. C. Carman, *Flow of Gases Through Porous Media*, Butterworths, London, 1956, 182 pp.

